

*This thesis is presented for the master's degree of Nagoya University*

# Estimation of galaxy SFRs from low radio frequencies

Shunraro YOSHIDA (ID:261801444)

March 2020

The laboratory of Galaxy Evolution ( $\Omega$  lab.)

Division of Particle and Astrophysical Science, Graduate School of Science  
Nagoya University, Japan

**Supervisors:** Prof. Dr. Tsutomu T. Takeuchi

Dr. Barbara Catinella

Dr. Luca Cortese

Dr. O. Ivy Wong



## Abstract

We present a global relation between the low-frequency and infrared (IR) emissions in star-forming galaxies compiled by the Herschel Reference Survey. The GaLactic Extragalactic All-sky MWA (GLEAM) survey operated by the Murchison Widefield Array (MWA) allows us to examine the relation and its frequency dependence with their 20 narrow bands at 72 – 231 MHz. These examinations are important for ensuring the reliability of the radio SFR. In this study, we focus on 18 star-forming galaxies whose radio emission is detected by the GLEAM survey. These galaxies show that a single power-law fitting is valid for understanding how the relation between the radio and IR luminosities varies across MWA frequencies to 1.5 GHz. We also investigate the consistency of the Star Formation Rate (SFR) calculated from the low-frequency emission with that from other indicators. Although this low-frequency emission has an advantage of the extinction-free indicator, the SFR calibration with averaged spectral parameters has a non-negligible uncertainty due to the variety of the radio to IR relation. We propose to use the individual spectral energy distribution for calculating the radio SFR for each star-forming galaxies with less uncertainty.

## Acknowledgments

I would like to thank Prof. Tsutomu T. Takeuchi, Dr. Luca Cortese, Dr. O. Ivy Wong and Dr. Barbara Catinella for their extraordinary support in my master's research. I would like to thank my colleagues also for their helpful and enjoyable discussion with me. You always supported me when I was suffering the research and my life. This project would have been impossible without the funding from Nagoya University (Overseas Challenge Program for Young Researchers 2019).

# Contents

<b>Contents</b>	ii
<b>List of Figures</b>	iv
<b>List of Tables</b>	v
<b>1 Introduction</b>	1
1.1 Star Formation Rate (SFR) . . . . .	1
1.2 Cosmic Star Formation History . . . . .	2
1.3 Low radio frequencies and SFR . . . . .	3
<b>2 Theoretical Background</b>	8
<b>3 Data</b>	9
3.1 Herschel Reference Survey (HRS) . . . . .	9
3.2 GLEAM survey . . . . .	11
<b>4 Methods</b>	13
4.1 Cross Matching . . . . .	13
4.2 Reduce galaxy samples for the secure analysis . . . . .	14
4.3 Calculating the $q_\nu$ parameter . . . . .	15
4.4 Total IR luminosity . . . . .	15
4.5 Fitting to $q_\nu$ parameters . . . . .	16
4.6 Calculating the SFR . . . . .	17
<b>5 Results</b>	18
5.1 Distributions of $\gamma$ . . . . .	18
5.2 Star Formation Rate (SFR) from the low-frequency emission . . . . .	19
<b>6 Discussions</b>	23
6.1 Comparing the calibration with previous results . . . . .	23
6.2 Radio SFR uncertainty . . . . .	23
<b>7 Summary</b>	25

<b>Bibliography</b>	<b>26</b>
<b>A Galaxy images</b>	<b>29</b>
A.1 Matched samples (18 samples used for the analysis) . . . . .	29
A.2 Matched samples (not used for the analysis) . . . . .	31
A.3 Suspicious matching samples . . . . .	31
A.4 Not matching samples . . . . .	31
<b>B Galaxy samples for the analysis</b>	<b>34</b>

# List of Figures

1.1	Reprint from Madau & Dickinson [2014] (Figure 9) . . . . .	3
1.2	Adapted from Helou et al. [1985] (Figure 2) . . . . .	4
1.3	Adapted from Kapińska et al. [2017] (Figure 5) . . . . .	5
1.4	Adapted from For et al. [2018] (Figure 6) . . . . .	6
3.1	Reprint from Boselli et al. 2010 (Figure 1) . . . . .	10
3.2	Reprint from Boselli et al. 2010 (Figure 2) . . . . .	11
3.3	Reprint from Hurley-Walker et al. 2017 (Figure 11) . . . . .	12
4.1	Separation from the cross-matching . . . . .	14
4.2	The comparison of total IR luminosities . . . . .	16
5.1	Histograms of $\gamma$ from the fitting . . . . .	18
5.2	The comparison of $\gamma$ from different fitting methods . . . . .	19
5.3	The consistency of the radio SFR . . . . .	20
5.4	The consistency of the radio SFR with $SFR_{IR}$ and $SFR_{FUV+24\text{mic}}$ . . . . .	21
A.1	Galaxy images (6/18 used for the analysis) . . . . .	29
A.2	Galaxy images (12/18 used for the analysis) . . . . .	30
A.3	Galaxy images (9/15 not used for the analysis) . . . . .	31
A.4	Galaxy images (6/15 not used for the analysis) . . . . .	32
A.5	Galaxy images (suspicious matching) . . . . .	32
A.6	Galaxy images (no matching) . . . . .	33

# List of Tables

B.1 The overview of 18 samples used for the analysis . . . . .	35
--	----

# Chapter 1

## Introduction

### ABSTRACT

Intro intro intro intro.

### 1.1 Star Formation Rate (SFR)

Star formation in galaxies is one of the most complex processes. In modern astronomy, understanding it and its evolution is still a challenging problem. To explain these, we need an advanced knowledge of dark matter and baryon physics. The evolution of dark matter is now interpreted by the “ $\Lambda$  CDM (Cold Dark Matter) model” which indicates structures in the universe have been forming hierarchically (bottom-up) [e.g., Peebles, 1982]. This model explains that a galaxy forms in a small dark halo once and merges into other halos to form larger systems as time goes on [Blumenthal et al., 1984]. With the advance of computational methods, a cosmological simulation can model this scenario and reproduce structures in the universe [e.g., Navarro & Steinmetz, 2000; Vale & Ostriker, 2004]. However, the baryon evolution inside dark halos is much more difficult to understand because its evolution attributes to the composition of different scale of physics. Revealing these physics needs as a first step to find constraints by measuring the star formation activity accurately. When we measure the star formation activity at each era in the universe, we can constrain the galaxy evolution scenario observationally (Section 1.2). The star formation rate (SFR) is the total mass of stars formed in a galaxy per year, and it is typically used for representing the star formation activity in a galaxy. SFR is one of the most fundamental and important values for understanding galaxy properties and its evolution.

Here, we present the SFR calibration methods. The fundamental equation to calculate SFR at time  $t$  from intrinsic stellar luminosity at wavelength of  $\lambda$  is shown below [Buat, 1991]:

$$L(\lambda, t) = \int_0^t \int_{M_{\text{low}}}^{M_{\text{up}}} F_\lambda(m, \theta) \text{SFR}(t - \theta) \psi(m) dm d\theta \quad (1.1)$$

where  $F_\lambda(m, \theta)$  is the evolutionary stellar tracks,  $\psi(m)$  is the Initial Mass Function (IMF; Chabrier 2003; Kroupa 2001; Salpeter 1955) and  $M_{\text{up}}$  ( $M_{\text{low}}$ ) is the upper (lower) limit of the stellar mass considered for the calculation.

Indeed, we can calculate SFR from Equation 1.1 in two ways. One way is to assume a certain stellar synthesis model and star formation history, and to calculate parameters to reproduce luminosities which we can observe at present. This method is called SED fitting and it is useful even for the galaxies experienced not stable star formation recently. However, this method highly depends on the star formation history chosen for the calculation.

Another way is to assume that SFR is constant over a certain timescale  $T$  and SFR is proportional to the luminosity. Although the timescale  $T$  depends on the wavelength for measuring, it is simple to calculate SFR with a specific luminosity. In this case, we can measure SFR with the following equation:

$$\text{SFR} = C \times L(\lambda) \quad (1.2)$$

where  $C$  is a constant.

This method is relatively easy to measure SFR from an observation, but the assumption of a constant SFR is sometimes problematic. Previous research show the required time to reach the steady state is  $\sim$  Myr for hydrogen recombination lines (e.g., H $\alpha$ ;  $\lambda = 6563\text{\AA}$ , H $\beta$ ;  $\lambda = 6563\text{\AA}$ ),  $\sim 100$  Myr for the Far-ultraviolet (FUV) to IR emissions [Hao et al., 2011; Kennicutt & Evans, 2012; Murphy et al., 2011]. These result show that the SFR calculated from Equation 1.2 is different from the true value if SFR varies among  $\sim 10$  Myr (e.g., Recent star burst).

Considering this problem, hydrogen recombination lines emitted by the young ( $\leq 10^7$  yr) and massive ( $M > 10 M_\odot$ ) OB stars are more reliable SFR indicators. However, in these cases, we should correct the dust extinction with the Balmer decrement which is the ratio between H $\alpha$  and H $\beta$  fluxes [Lequeux et al., 1981], or with IR luminosities [Kennicutt et al., 2009]. In addition to this, we need to eliminate [NII] line contamination ( $\lambda = 6548\text{\AA}, 6584\text{\AA}$ ) from H $\alpha$  emission, and correct the absorption of H $\beta$  by the young stellar atmosphere. Although recombination lines are good SFR indicator in terms of the time scale in a constant star formation, the calibration for them gives us non-negligible uncertainty.

FUV emission is emitted by the A (or B) stars and it is reliable as SFR indicator if the star formation timescale can be assumed more than  $10^8$  yr. Because of its wavelength (*GALEX* FUV;  $1516\text{\AA}$ ), we need to correct the dust extinction also for FUV. We often use IR luminosities for the dust correction based on the idea that dust grains absorbing FUV light re-emits it at a wavelength range of IR [Kennicutt, 1998; Murphy et al., 2011]. The combination of FUV and IR emissions for estimating SFR is one of the most popular SFR indicators (e.g., FUV + 24mic, FUV + total IR).

Besides these indicators, in this study, we focus on the low-frequency radio emission around  $\sim 100$  MHz because it is also a SFR indicator guaranteed by its correlated with (Far) IR emissions and SFR in galaxies (Section 1.3).

## 1.2 Cosmic Star Formation History

Tinsley & Danly [1980] proposed the cosmic star formation history which shows the SFR density evolution in the universe. While no one could observe much more high-z galaxies enough to do the statistics at that time, we can now observe intrinsic FUV and IR luminosities from a large number

of galaxies up to  $z \sim 4$  (and up to  $z \sim 7$  with only ultraviolet). Recent studies [Hopkins & Beacom, 2006; Madau & Dickinson, 2014] make a cosmic star formation history with a consistent IMF over all the redshift range. Their plots represent that the peak of the star formation happened at  $z \sim 1.9$  where 3.5 Gyr after the Big Bang (Figure 1.1). The era when the SFR density was the highest is called “Cosmic Noon” because the star formation in the universe was the most active. The era before Cosmic Noon ( $z > 1.9$ ) is called “Cosmic dawn”.

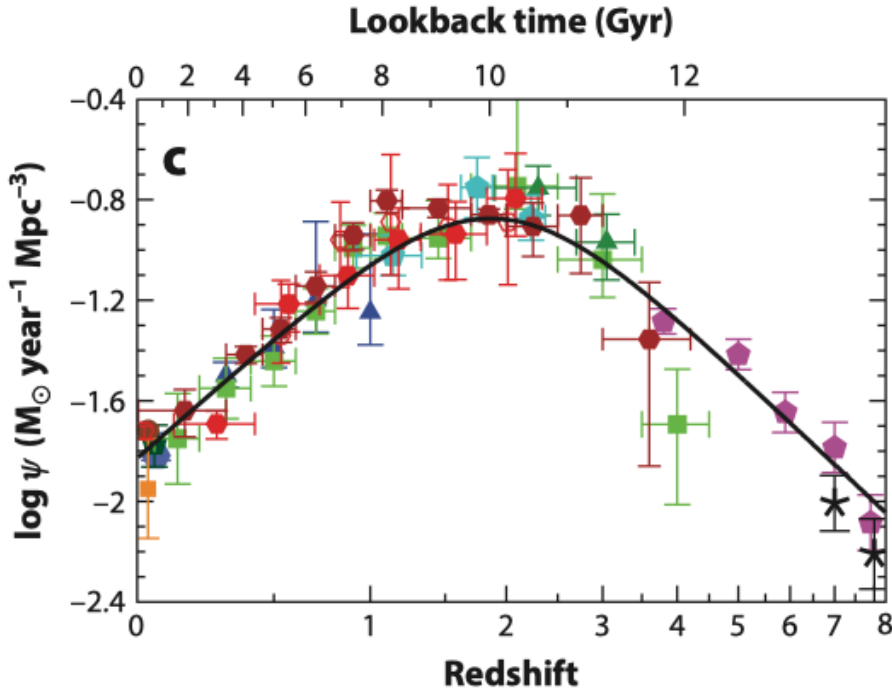


**Figure 1.1:** (Reprint from Madau & Dickinson [2014], Figure 9)

This figure shows the cosmic star formation history from UV and IR emissions. For calculating SFR, they adopt Salpeter IMF. The black solid line shows the best fitting line. We can see the peak of SFR density in the universe at  $z \sim 1.9$

Although now we know the cosmic star formation history up to  $z \sim 8$  ( $z > 4$  is still ambiguous due to the lack of IR observation), extending it to the earlier universe is quite difficult because we do not have a telescope to observe IR luminosity from high-z galaxies with a large field of view. FUV emission from high-z galaxies is also difficult to be calibrated because the dust correction for high-z galaxies still have a large uncertainty.

On the contrary, the low-frequency emission is a extinction-free estimator and we will be able to observe high-z galaxies with a high sensitivity and large field of view enough to extend the cosmic star formation history.

### 1.3 Low radio frequencies and SFR

The low-frequency radio emission from star-forming galaxies has been studied for many years. In this paper, we use the term “Low frequency” as the frequency of a few GHz and less than that. The importance of this emission increased after the global log-linear correlation with infrared (IR) had been found. This correlation was discovered by Helou et al. [1985] using integrated far-infrared (FIR; 60  $\mu\text{m}$

and  $100 \mu\text{m}$ ) and 1.4 GHz radio luminosities in star-forming galaxies (Figure 1.2). Although this correlation is originally called FIR-Radio Correlation, we use the term “IR-Radio Correlation (IRC)” because we tend to examine the correlation of radio with the total IR luminosity instead of FIR after Bell [2003].

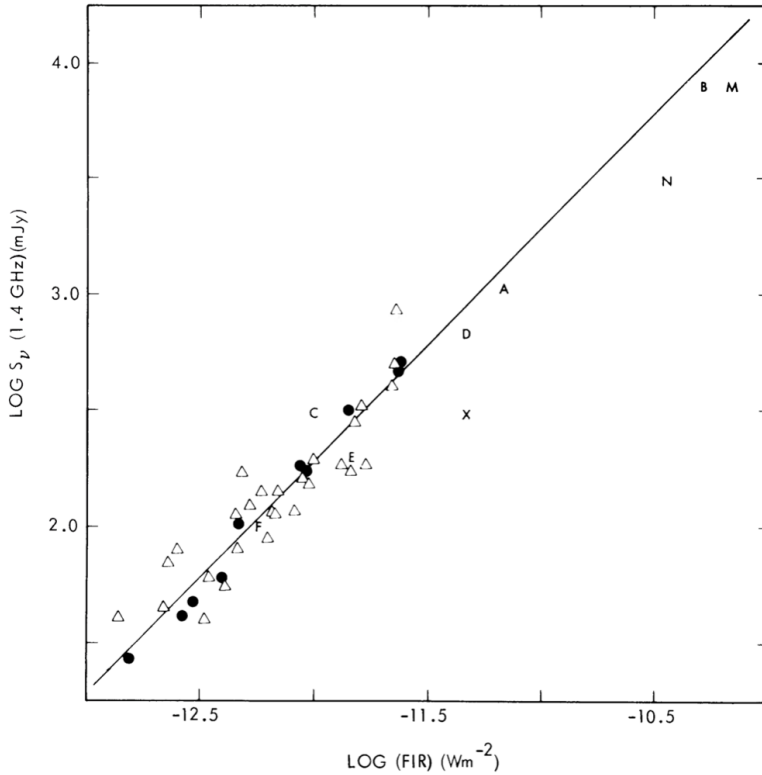


**Figure 1.2:** (Adapted from Helou et al. [1985], Figure 2)

This figure shows the comparison between FIR and radio at 1.4 GHz fluxes for each galaxy. We can see the tight correlation between them.

Bell [2003]; Condon et al. [1991]; Yun et al. [2001] have examined this global correlation using a different sample set and found it holds the tightness across more than three orders of magnitude. Recently, the low-frequency survey at around 100 MHz was operated by the LOw Frequency Array (LOFAR; van Haarlem et al. 2013) and the Murchison Widefield Array (MWA; Tingay et al. 2013). With the advent of these telescopes, Calistro Rivera et al. [2017]; Read et al. [2018]; Wang et al. [2019] extend the study to at an order of magnitude lower frequency and find the correlation is held at not only 1.4 GHz but also  $\sim 100 \text{ MHz}$ . Thanks to this correlation, we can regard the low frequency emission as a SFR indicator because IR luminosity is emitted by heated dust grains in a galaxy and can measure the SFR. Since the low-frequency emission is not affected by the dust extinction [Murphy et al., 2011; Yun et al., 2001] and it will be observed from a distant galaxies by the future extended survey, we anticipate its usefulness and need a further investigation of the relation between the radio and IR luminosities, especially its frequency dependence.

To explain IRC physically, Völk [1989] proposed “the calorimeter model”. This model says that all energies from high energy electrons consumed before they escaping from galaxies is linearly correlated with all energies re-radiated as IR emissions by dust absorbing all FUV emission from young stars.

However, the spatially-resolved studies show that a star-forming galaxy emits the radio emission

whose spectral index depends on the galaxy region [For et al., 2018; Heesen et al., 2019; Kapińska et al., 2017] (Figure 1.3 and 1.4). This means that the radio emission is sensitive to the local density environment of the ISM and it is not guaranteed a simple frequency dependence of the global relation between the integrated radio and IR luminosities.

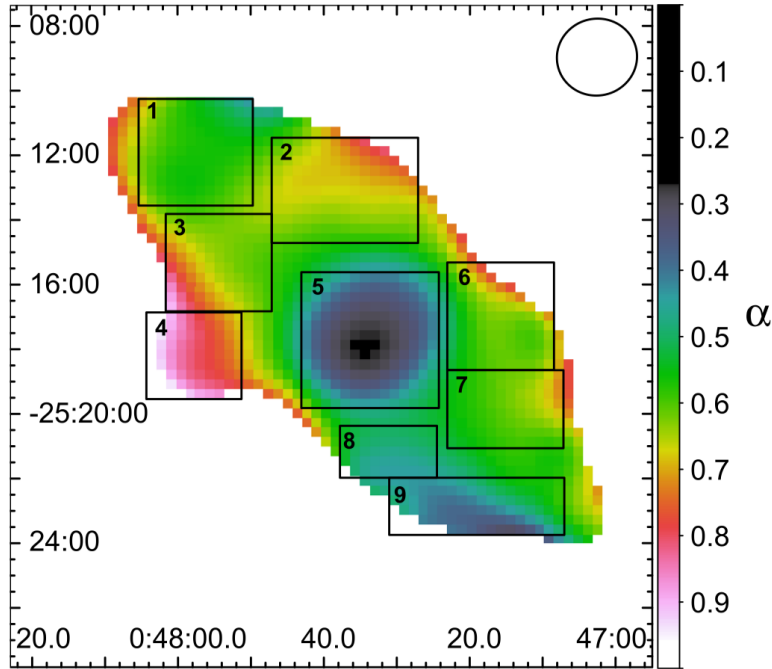


**Figure 1.3:** (Adapted from Kapińska et al. [2017], Figure 5)

This figure shows the distribution of the radio spectral index in NGC 253. They do the fitting between 200 MHz (GLEAM; Hurley-Walker et al. 2017) and 1.465 GHz [Carilli et al., 1992]. The color scale is for the spectral index and the pixel size is  $18 \times 18 \text{ arcsec}^2$ .

The integrated radio emission in star-forming galaxies across 100 MHz to 1.4 GHz is supposed to compose of a few percent to 10% free-free and the synchrotron radiations [Condon, 1992]. Each radiation is emitted by electrons interacted with the electric field of ions in the HII region or the magnetic field in a galaxy. For emitting the synchrotron radiation, an electron needs to be accelerated to the light speed by the supernova remnant. While the synchrotron emission is expected to be dominant at these low frequencies, previous studies find the sign of the free-free absorption and flatter or turnover spectral [Chyží et al., 2018; Schober et al., 2017]. If the radio emission has a significant turnover among low frequencies, IRC does not have a simple frequency dependence and the radio emission is no longer useful as a SFR indicator.

In this study, we investigate nearby star-forming galaxies from the reference sample for ensuring the reliability of measuring the SFR from the low-frequency emission. For examining the general trend, we use star-forming galaxy samples from Herschel Reference Survey (HRS; Boselli et al. 2010) catalog which are supposed to represent the galaxy samples and the low-frequency emission from The Galactic Extragalactic All-sky MWA (GLEAM; Hurley-Walker et al. 2017) Survey which observes the mJy scale radio emission from large areas with their 20 narrow bands.

This paper is organized as follows. In Chapter 3, we introduce our galaxy samples and the low-frequency emissions used in this study. In Chapter ??, we introduce the IR-Radio Correlation with

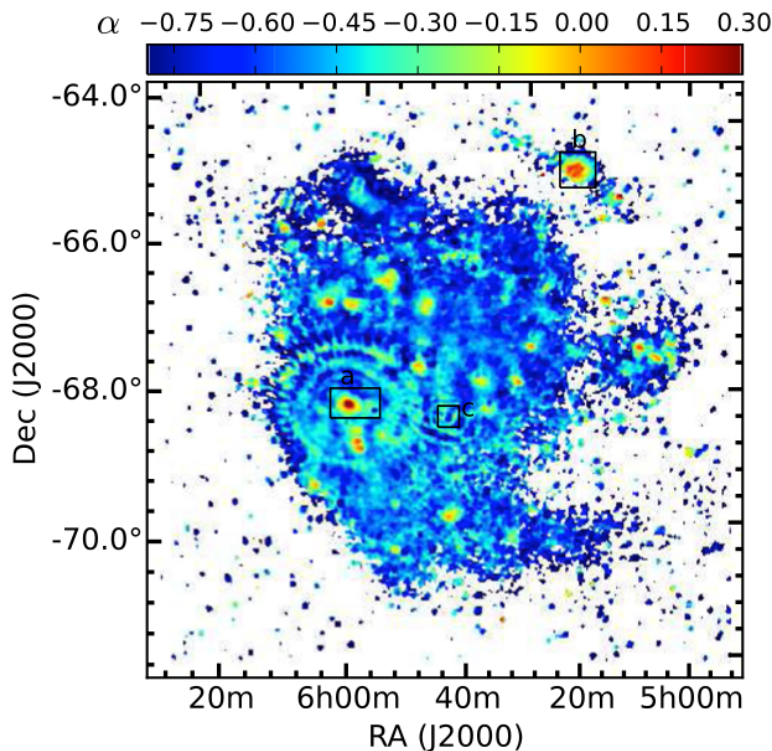


**Figure 1.4:** (Adapted from For et al. [2018], Figure 6)

This figure shows the distribution of the radio spectral index in Large Magellanic Could (LMC). They do the fitting between 166 MHz (GLEAM; Hurley-Walker et al. 2017) and 1.4 GHz [Hughes et al., 2007]. The color scale is for the spectral index and the pixel size is  $34.9 \times 34.9 \text{ arcsec}^2$  at GLEAM 166MHz.

the  $q_\nu$  value defined for evaluating the correlation quantitatively. Here, we also mention the way to investigate its frequency dependence and derive the radio SFR. In Chapter 5, we show our results about the frequency dependence of IRC and the consistency of the radio SFR. In Chapter 6, we compare our results with previous studies. Finally, we summarize our study in Chapter 7.

## Chapter 2

# Theoretical Background

### **ABSTRACT**

Intro intro intro intro.

Here, I will describe synchrotron emissions?

# Chapter 3

## Data

### ABSTRACT

In this chapter, I describe the dataset used for our study.

### 3.1 Herschel Reference Survey (HRS)

In this section, I introduce the Herschel Reference Survey (HRS) catalog [Boselli et al., 2010]. This survey is one of the Herschel guaranteed time key projects and originally it was compiled for understanding dust properties and interstellar medium in nearby galaxies. The catalog contains 322 galaxies selected with the three following criteria.

#### 1. Volume-limited:

They choose galaxies whose distance from the earth is between 15 and 25 Mpc. This limitation reduce the distance uncertainty due to the galaxy peculiar motions and the selection effect due to the high-z galaxies. The lower limit (15 Mpc) also helps us to observe sources within the reasonable exposure time because galaxies too close to us are extended and we need too much time for the observation.

#### 2. *K*-band selection:

They choose galaxies whose 2MASS *K*-band total magnitudes are less than 12 mag for star-forming and peculiar galaxies (Sa-Sd-Im-BCD), and 8.7 mag for quiescent galaxies (E, S0, S0a). If there are galaxies whose *K*-band magnitude more than those values, their measurements are not regarded as an accurate photometry because of not enough exposure time. The reason why they have selected quiescent galaxies with the more stringent *K*-band selection criteria is these galaxies are expected to have low dust contents, and it is difficult to detect within the reasonable exposure time.

#### 3. High galactic latitude:

They choose galaxies whose galactic latitude is high enough to minimize the contamination from the galactic center ( $b > +55^\circ$ ). Also, they have selected galaxies with the low galactic extinction ( $A_B < 0.2$ ; Schlegel et al. 1998).

The selected galaxies located in the sky region between  $10^{\text{h}}17^{\text{m}} < \text{R.A.(2000)} < 14^{\text{h}}43^{\text{m}}$  and  $-6^{\circ} < \text{decl.} < 60^{\circ}$  (Figure 3.1) HRS galaxies spans a large range of the galaxy density environment from the center of Virgo cluster to the isolated region. As a definition, we can regard the HRS sample as a ideal one for studying the galaxy environment.

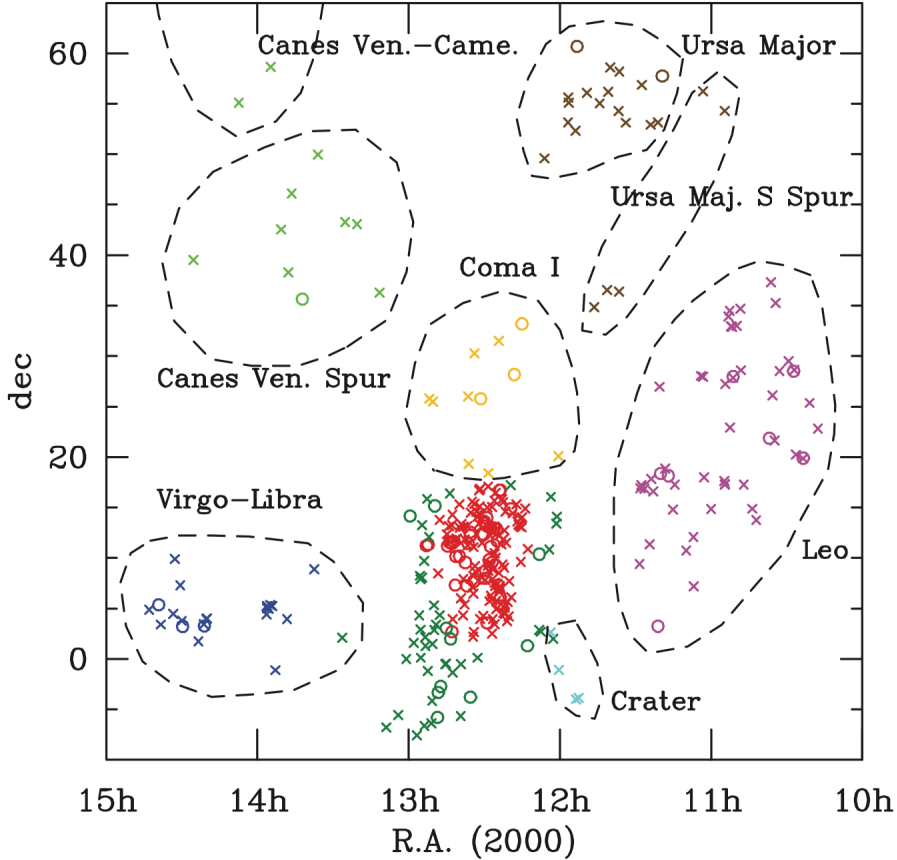


**Figure 3.1:** (Reprint from Boselli et al. 2010, Figure 1)

This figure shows the sky distribution of HRS galaxy samples. They show the early-type galaxies (E, S0, S0a) and late-type galaxies with circles and crosses, respectively. Dashed circles represents the different cloud regions. Each name of the cloud is shown close to each region. The red and dark green markers are Virgo galaxies (red: Virgo center, dark green: its outskirts).

In addition to a large range of the environment, the HRS galaxies distribute a wide range of the galaxy morphology (Figure 3.2).

Since HRS galaxies are supposed to be well-represented for the whole galaxy population located in the local universe, understanding their physical properties is a critical study. After Boselli et al. [2010] published the HRS sample, many studies investigating the physical properties for HRS galaxies have been done until now. Here, I introduce some of the studies for the HRS sample. Cortese et al. [2012] investigated their UV and optical properties using the Galaxy Evolution Explorer (GALEX; Martin et al. 2005) and SDSS-DR7 [Abazajian et al., 2009]. Boselli et al. [2014] studied their cold gas properties with  $^{12}\text{CO}$  ( $1 - 0$ ) observed by the Kitt Peak 12m radio telescope and obtained from the literature data. They also investigate the HI gas obtained from The Arecibo Legacy Fast ALFA (ALFALFA; Giovanelli et al. 2005; Haynes et al. 2011) Survey. Ciesla et al. [2014] executed the SED fitting for HRS galaxies with Code Investigating GALaxy Emission (CIGALE; Noll et al. 2009).

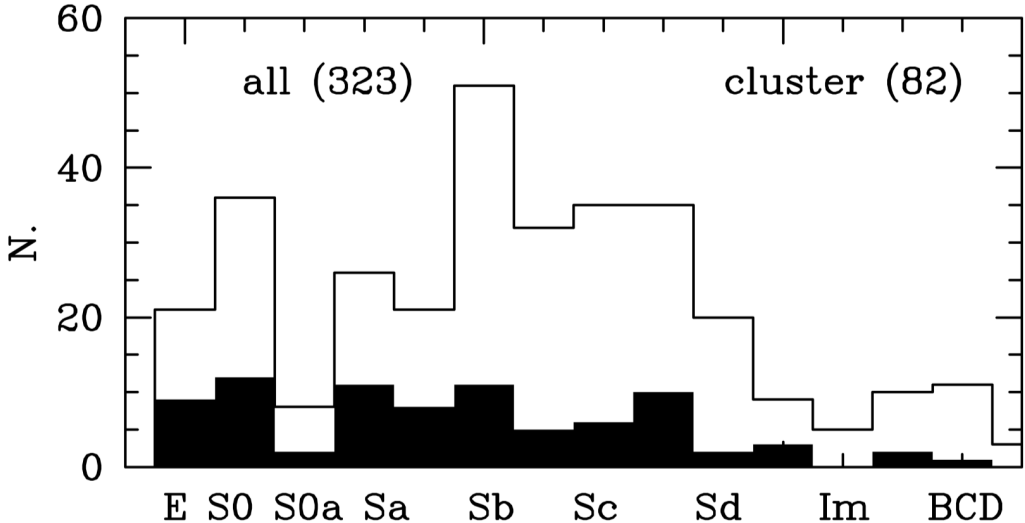


**Figure 3.2:** (Reprint from Boselli et al. 2010, Figure 2)

This figure shows the distribution in the morphology-type of HRS galaxies. The shaded histogram represents the distribution in it of only the cluster sample. Here, the cluster sample composed of HRS galaxies located in the Virgo A and B clouds.

Thanks to all of previous research about the HRS sample, they are well-studied among the wide range of the wavelength from the X-ray to the radio emission at 1.5 GHz. However, the low-frequency around 100 MHz is not examined so far. In this study, we focus on a subsample of HRS galaxies, whose counterpart is detected by the latest low-frequency survey (Section 3.2).

## 3.2 GLEAM survey

In this section, I introduce the GaLactic Extragalactic All-sky MWA (GLEAM) survey [Hurley-Walker et al., 2017]. This survey was operated by the Murchison Widefield Array (MWA) telescope [Tingay et al., 2013] in Western Australia. It observed a whole southern sky and a northern sky up to  $+30^\circ$  ( $\sim 25,000$  deg $^2$ ; Figure 3.3). The catalog from this survey is a publicly-available and contains 307,455 detected radio sources with fluxes at 20 narrow bands between 72 and 231 MHz (each band has 7.68 MHz band width). The sensitivity and angular resolution at 200 MHz are  $\sim 7$  mJy and  $\sim 2$  arcmin respectively. The completeness of this survey at 200 MHz is 90% at  $\sim 170$  mJy. Since this survey allows us to examine the low-frequency spectral energy distribution accurately with their 20 narrow bands, we adopt the radio source catalog for our study.

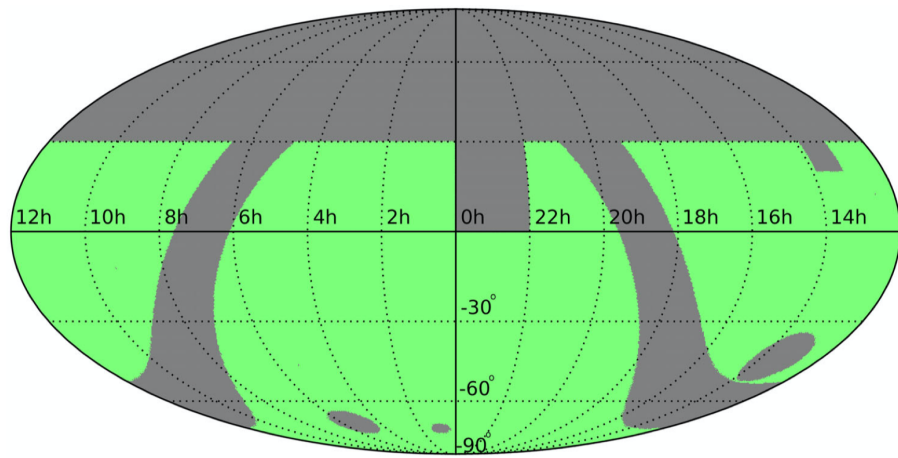


**Figure 3.3:** (Reprint from Hurley-Walker et al. 2017, Figure 11)

This figure shows the observed area by the GLEAM survey (green shaded region). They exclude several regions intentionally to minimize the contamination: Galactic plane (Absolute Galactic latitude  $< 10^\circ$ ), Ionospherically distorted ( $0^\circ < \text{Dec} < +30^\circ$  and  $22^\text{h} < \text{R.A.} < 0^\text{h}$ ), Centaurus A ( $13^\text{h}25^\text{m}28^\text{s} - 43^\circ01'09''$ ,  $r = 9^\circ$ ), Sidelobe reflection of Cen A ( $20^\circ < \text{Dec} < +30^\circ$  and  $13^\text{h}07^\text{m} < \text{R.A.} < 13^\text{h}53^\text{m}$ ), Large Magellanic Cloud ( $05^\text{h}23^\text{m}35^\text{s} - 69^\circ45'22''$ ,  $r = 5.5^\circ$ ) and Small Magellanic Cloud ( $00^\text{h}52^\text{m}38^\text{s} - 72^\circ48'01''$ ,  $r = 2.5^\circ$ ).

# Chapter 4

## Methods

### ABSTRACT

Intro intro intro intro.

### 4.1 Cross Matching

Although HRS galaxies have been studied in multi-wavelength observations, their spectral energy distribution around 100 MHz is not well-understood, where the contribution from synchrotron radiation is much more significant than from free-free emission [Condon, 1992]. Here, I provide a procedure to cross-matching with two different catalogs I have mentioned in the previous chapter. Cross-matching is the method widely used in astronomy to obtain additional information from other surveys or catalogs by matching coordinates of each galaxy or blob source within a specific error (e.g.,  $\sim 1$  arcsec). For executing this method for the HRS and the GLEAM survey catalog, we use Tool for OPerations on Catalogues And Tables (TOPCAT; Taylor et al. 2009). TOPCAT is popular and an useful tool for dealing with catalogs and tables, and it allows us to do the cross-matching easily, even more than two catalogs.

Initially, we assume a 10 arcsec error radius for the cross-matching since it is equivalent to the value of 95% error for the astrometry in the GLEAM survey (Section 4.5.5 in Hurley-Walker et al. 2017). This matching results in a total of 18 galaxies which are identified to have a radio counterpart. To assess the matching, we compare a separation of counterparts from the center of galaxies with coordinate uncertainties in the GLEAM catalog. For these galaxies, we find 15 of them have a separation within a 95% error radius, and others do not. Although three of them have a larger separation compared to the error radius, we conclude that the matching for all 18 galaxies is correct by the checking of galaxy images (Appendix A). In this paper, we regard a radio blob as a counterpart if the brightest part of each blob where the inside of the contour nearest to the center, is surrounded by the D25 radius (the isophotal optical size at 25 mag arcsec $^{-2}$ ; Boselli et al. 2010).

Next, we extend the error radius up to 120 arcsec, which is corresponding to the angular resolution of the GLEAM survey at 200 MHz. This is because the radio sources are blurred due to the angular resolution of the GLEAM survey and the location of them might be shifted. We know 120 arcsec error radius is quite big for the matching, but this trial gives us the inspiration for the cross-matching with

blurred radio sources in the future study. The cross-matching with the error of 120 arcsec suggests that there are 25 new galaxies have a potential counterpart. To assess these matching, we look at galaxy images one by one (All galaxy images are in Appendix A). With the same condition mentioned above, we identify 21 matches for these galaxies.

Although we have identified a total of 39 matches in the same way, there are six suspicious matches because of interacting counterparts (HRS4, 216, 244, 284) and quite large separations (HRS200, 295) (Figure A.5). For these galaxies, we flag them as suspicious matches, and we do not use them for further analysis. The distribution of separations for galaxies showed in Figure 4.1.

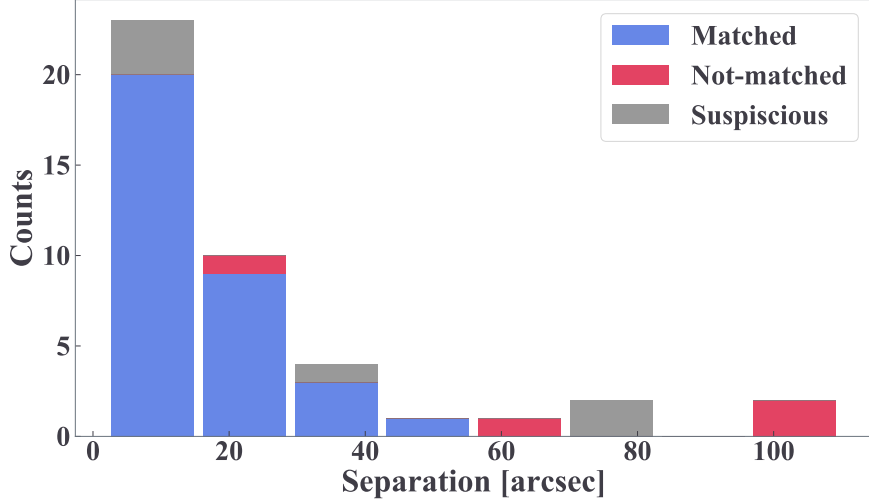


**Figure 4.1:** This figure shows the distribution of separations. Here we put 43 galaxies and color sorted based on the result. The blue bar shows galaxies identified to have a radio counterpart, red one does galaxies determined not to have a counterpart, and gray for the suspicious galaxies. Most of the matched samples are distributed within a 40 arcsec error radius.

We put all galaxy images cross-matched within 120 arcsec in Appendix A.

## 4.2 Reduce galaxy samples for the secure analysis

In this section, we show some steps for selecting galaxies to do a secure analysis. Since we focus on the relation of galaxy radio emission with star formation activities, we should clarify the radio source and be sure that they are not originally from other sources rather than the star formation. The radio emission arisen from the star formation activities should be proportional to the SFR in a galaxy [Condon, 1992; Murphy et al., 2011]. However, elliptical galaxies have a stronger radio emission against their star formation, in this case their radio emission would be emitted by non star-forming sources. These radio sources are considered as Active Galactic Nuclei (AGN), which emits strong radio emission due to the baryon accretion into the supermassive black hole at the center of galaxies irrelevant to the star formation [e.g., Padovani et al., 2017; Urry & Padovani, 1995]. According to the morphology of galaxies [Cortese et al., 2012], we identify four elliptical galaxies (HRS49, 138, 178, 241) and not use for further calculation and discussion.

After this galaxy selection, we obtain 29 galaxies with a reliable radio counterpart arisen from the star formation activity.

As a next step, we evaluate the signal to noise ratio (SNR) of radio emission at each MWA band. For reducing the uncertainty caused by observational errors, we assess the peak flux at each narrow band by comparing it to the local noise level and adopt flux values whose SNR is higher than five. This analysis results in a total of 11 galaxies have no radio fluxes whose SNR is higher than the criterion. The reason why these radio sources are detected, although they do not have any fluxes with higher SNR, is Hurley-Walker et al. [2017] determine the detection based on the SNR in the stacking images (170 – 231 MHz).

Finally, after the cross-matching and these procedures, we confirm 18 HRS galaxies are the samples available for further analysis. The overview of 18 samples is tabled in Appendix B.

### 4.3 Calculating the $q_\nu$ parameter

In this section, I introduce the method to calculate  $q_\nu$  parameter for each galaxy. The definition of this parameter here is given on the following equation [e.g. Bell, 2003; Calistro Rivera et al., 2017; Helou et al., 1985]:

$$q_\nu \equiv \log \left( \frac{L_{8-1000\mu\text{m}} / 3.75 \times 10^{12}}{\text{erg s}^{-1} \text{Hz}^{-1}} \right) - \log \left( \frac{L_{\text{Radio},\nu}}{\text{erg s}^{-1} \text{Hz}^{-1}} \right) \quad (4.1)$$

where  $L_{8-1000\mu\text{m}}$  is the total rest-frame infrared luminosity among 8–1000  $\mu\text{m}$ , which reflects the total dust luminosity, and  $3.75 \times 10^{12}$  is equivalent to the frequency of 80  $\mu\text{m}$  for correcting the dimension.

Although Ciesla et al. [2014] have already derived the total IR luminosity for most HRS galaxies using the SED fitting, one of our galaxy samples (HRS163) does not have the value because of the lack of the reliable mid IR flux from *Spitzer* telescope. For consistency, we adopt the total IR luminosity calculated from the same method for all galaxy samples. To calculate the total IR luminosity, we refer to Galametz et al. [2013], which derive the calibration relation between combining monochromatic IR luminosities and the total IR luminosity. We show the procedure to calculate total IR luminosity in the next section.

### 4.4 Total IR luminosity

In this section, I present how to calculate the total IR luminosity. For the method of calculating total IR luminosity, we refer to Galametz et al. [2013], which shows the empirical relations to estimate total IR from *Spitzer* (24, 70  $\mu\text{m}$ ) and *Herschel* bands (100, 160, 250  $\mu\text{m}$ ). HRS galaxies have flux data from the Multiband Imaging Photometry for *Spitzer* (MIPS; Bendo et al. 2012; Rieke et al. 2004), the *Herschel*/PACS (100, 160  $\mu\text{m}$ ; Cortese et al. 2014) and the *Herschel*/SPIRE (250  $\mu\text{m}$ ; Ciesla et al. 2012).

Galametz et al. [2013] derived the calibration equation below:

$$L_{3-1100\mu\text{m}} = \sum c_i \nu L_\nu (i) \quad (4.2)$$

where  $L_{3-1100\mu\text{m}}$  is the total IR luminosity in the frequency range from 3 to  $1100\mu\text{m}$ ,  $c_i$  is the coefficients at  $i = 24, 70, 100, 160, 250\mu\text{m}$ , and  $L_\nu$  is the luminosity at the frequency  $\nu$  corresponds to a specific wavelength  $i$ . For deriving  $L_\nu$ , we calculate it from fluxes and the distance to each galaxy. We refer to Cortese et al. [2012] for obtaining galaxy distances.

Galametz et al. [2013] derived the conversion equation with at least two bands. Therefore, we can estimate total IR luminosities even if galaxies are lack of a few fluxes. Since several calculations in the following sections require the total IR luminosity among  $8 - 1000\mu\text{m}$  ( $L_{8-1000\mu\text{m}}$ ), we recalibrate this luminosity by multiplying the constant value (0.88) in Takeuchi et al. [2005].

The total IR luminosity calculated here is consistent with that of Ciesla et al. [2014] within factor 2 (Figure 4.2).

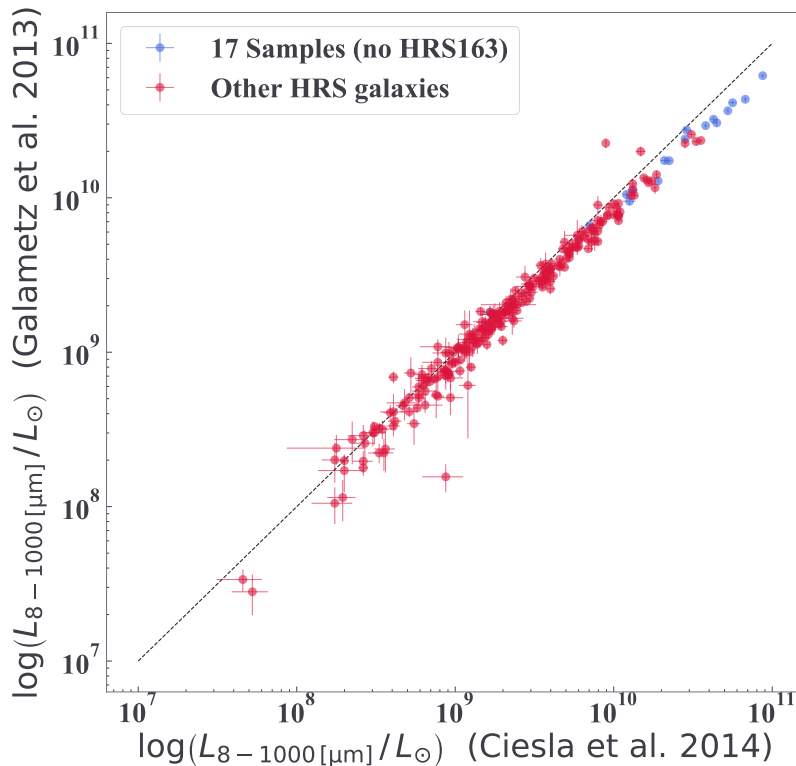


**Figure 4.2:** This figure shows the comparison of total IR luminosity at  $8 - 1000\mu\text{m}$  from different methods. Here, we show all HRS galaxies which have both luminosities. Blue plots show galaxy samples selected in Section 4.1 and 4.2, and red ones show other HRS galaxies. The difference of both luminosities is less than factor 2.

Hereafter, we use  $L_{8-1000\mu\text{m}}$  obtained here to calculate the  $q$  parameter and SFR.

## 4.5 Fitting to $q_\nu$ parameters

Here, we show how to do the fitting to  $q_\nu$ . At low frequencies around 100 MHz, the synchrotron emission can be dominant, which emitted from high energy electrons accelerated by the supernova

remnant. In this paper, we assume radio emission has a single power-law on the frequency and adopt the following equation:

$$q_\nu = -\gamma \log \nu + \beta \quad (4.3)$$

where  $q_\nu$  is defined by Equation 4.1 at  $\nu$  MHz,  $\gamma$  is the power-law index showing the frequency dependence of  $q_\nu$  and  $\beta$  is the second fitting parameter.

In this study, we execute two types of fitting:

1. Fitting to only MWA frequencies (72 – 231 MHz)
2. Fitting to 1500 MHz besides MWA frequencies

The flux data at 1500 MHz is obtained from Boselli et al. [2015], and here we use only high-quality flux data (flag = 1). These two types of fitting might allow us to judge the correctness of a single power-law assumption. These fitting results are summarized in Section 5.1.

## 4.6 Calculating the SFR

In this section, I describe how to derive SFR from low-frequency radio emissions.

Here, we estimate the radio SFR, combining Equation 4.1 with the following equations:

$$\text{SFR}_{\text{IR}} = 3.88 \times 10^{-44} \left( \frac{L_{8-1000\mu\text{m}}}{\text{erg s}^{-1}} \right) \quad (4.4)$$

$$q_{\nu \text{ MHz}} = q_{1500 \text{ MHz}} + \log \left( \frac{\nu \text{ MHz}}{1500 \text{ MHz}} \right)^\gamma \quad (4.5)$$

Equation 4.4 calculates SFR from the total IR emission in Murphy et al. [2011], and Equation 4.5 shows the difference of the  $q_\nu$  between a certain wavelength  $\nu$  and 1500 MHz.

Substituting equation 4.1 and 4.5 into equation 4.4 yields the following equation to estimate SFR from radio emission at  $\nu$  MHz:

$$SFR_{\text{Radio}, \nu} = 1.46 \times 10^{-31} \times 10^{q_{1500 \text{ MHz}}} \left( \frac{\nu \text{ MHz}}{1500 \text{ MHz}} \right)^{-\gamma} \times L_{\text{Radio}, \nu} \quad (4.6)$$

In Section 5.2, I show the results of calculating SFR from the low-frequency radio using this equation and comparing it with the SFR from other indicator.

# Chapter 5

## Results

### ABSTRACT

In this chapter, we present our results with figures. Firstly, in Section ??, we show the  $q_\nu$  frequency dependence for each galaxy with the distribution of  $\gamma$ . Secondly, in Section 5.2, we show the result of the comparison between the SFR from a radio emission and other indicators.

### 5.1 Distributions of $\gamma$

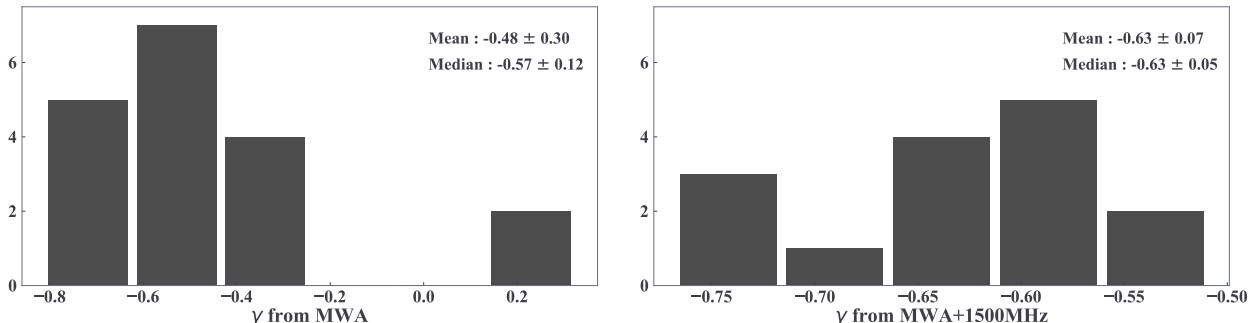


**Figure 5.1:** This figure shows distributions of  $\gamma$  for each fitting. The left figure indicates the fitting result with only MWA frequencies, and the right one does with 1500 [MHz] besides MWA frequencies.

Here, we show two kinds of fitting results. The left plot in Figure 5.1 is the  $\gamma$  distribution from the fitting only to MWA frequencies, and the right one is to 1500 MHz besides MWA frequencies. We show the mean and median with the standard and quantile deviation in both plots. Since we adopt high-quality flux data at 1500 MHz [Boselli et al., 2015], three samples (HRS 122, 163 and 204) are fitted only in the case with MWA fluxes. Figure 5.2 compares  $\gamma$  from different fitting fluxes for each galaxy.

In these figures, we can find that there are two galaxies (HRS 25 and 144) with a relatively flatter  $\gamma$  fitted only to MWA frequencies. This suggests that there is a critical frequency where the turnover arises between MWA frequencies and 1500 MHz. At low frequencies, the spectral is prone to be flatter due to the free-free absorption [e.g., Calistro Rivera et al., 2017; Chyzy et al., 2018; Schober et al.,

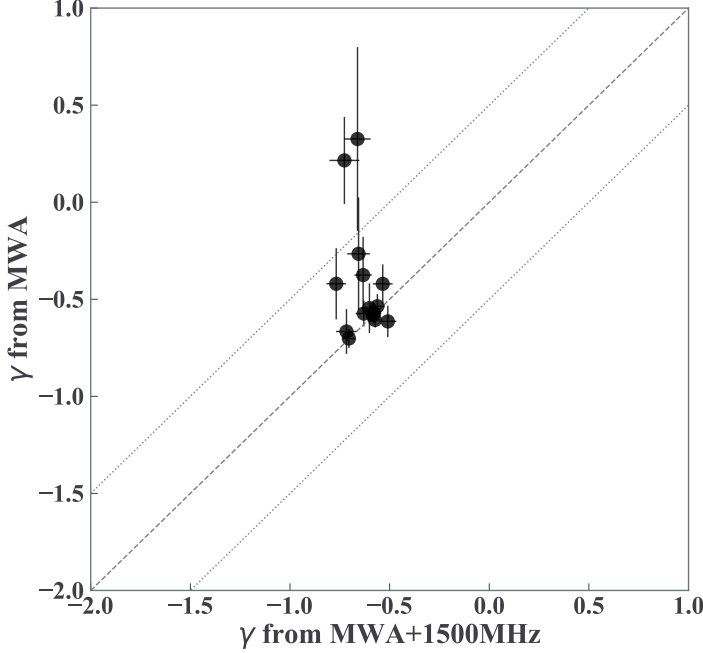


**Figure 5.2:** This figure is for comparing the difference of  $\gamma$  for each fitting method. The solid line shows the one to one correlation, and dotted lines show 0.5 dex away from the solid line. Each plot shows each galaxy. In this figure, we can see  $\gamma$  fitted to only MWA frequencies are relatively flatter.

2017]. In addition to this, Schober et al. [2017] show that a Milky Way like galaxy (similar SFR) has the critical frequency order of magnitude lower than the MWA frequency. However, HRS 25 and 144 have a Milky Way like SFR [Boselli et al., 2015] and a critical frequency between MWA frequencies and 1500 MHz. This result cannot be explained by Schober et al. [2017]. One possible explanation is that fewer number of fluxes yields less constraint of the fitting and the flatter  $\gamma$  for HRS 25 and the galactic nuclei affects the spectral for HRS 144 identified as a Seyfert galaxy from the BPT diagram [e.g., Baldwin et al., 1981; Kauffmann et al., 2003; Kewley et al., 2001; Schawinski et al., 2007]. For understanding these galaxies, we would need the case study with more data in a wide frequency range.

If we neglect these galaxies, the mean  $\gamma$  changes from  $-0.48 \pm 0.30$  to  $-0.57 \pm 0.14$  for the fitting without 1500 MHz and from  $-0.63 \pm 0.08$  to  $-0.62 \pm 0.08$  with 1500 MHz. The mean  $\gamma$  does not vary in any case with 1500 MHz. This means that HRS 25 and 144 do not affect the fitting result among MWA frequencies and 1500 MHz, although they do the mean  $\gamma$  from the fitting only to MWA frequencies. Therefore, in this paper, we adopt the averaged  $\gamma$  obtained from the fitting across the MWA frequency to 1500 MHz for calculating SFR (Section 5.2).

The fitting results are shown in Appendix ??.

## 5.2 Star Formation Rate (SFR) from the low-frequency emission

Here, we show the result from comparing  $SFR_{\text{Radio}, \nu}$  defined by Equation 4.6 with  $SFR_{\text{IR}}$  (Equation 4.4) and  $SFR_{\text{FUV}+24\text{mic}}$  [Boselli et al., 2015].

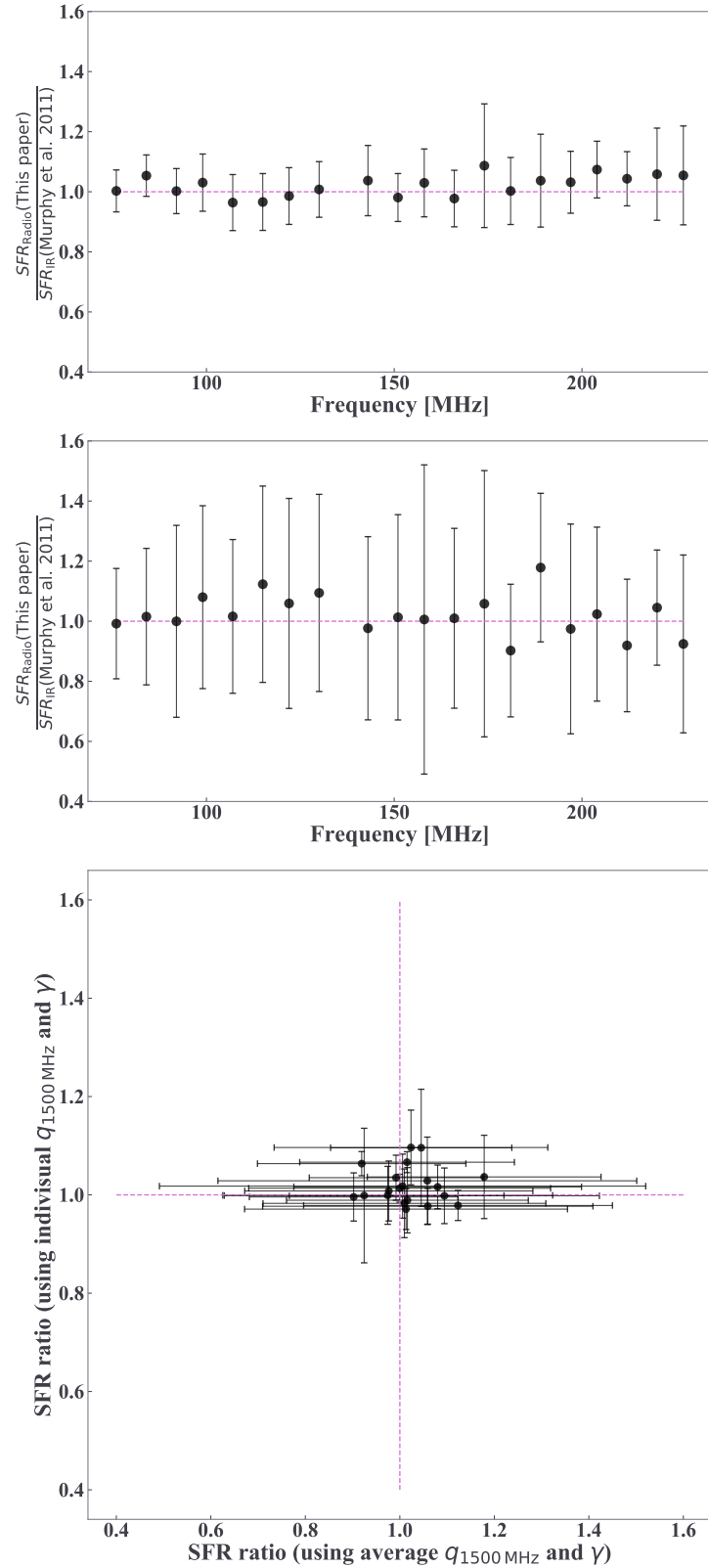


**Figure 5.3:** This figure shows the SFR ratio between  $SFR_{\text{Radio},\nu}$  and  $SFR_{\text{IR}}$  at each MWA frequency. The difference between the upper and middle plots is the calibration parameters to calculate  $SFR_{\text{Radio},\nu}$ . Individual or averaged  $\gamma$  and  $q_{1500 \text{ MHz}}$  are used for the upper or middle plots, respectively. The bottom plot compares SFR ratios calculated with different calibrations.

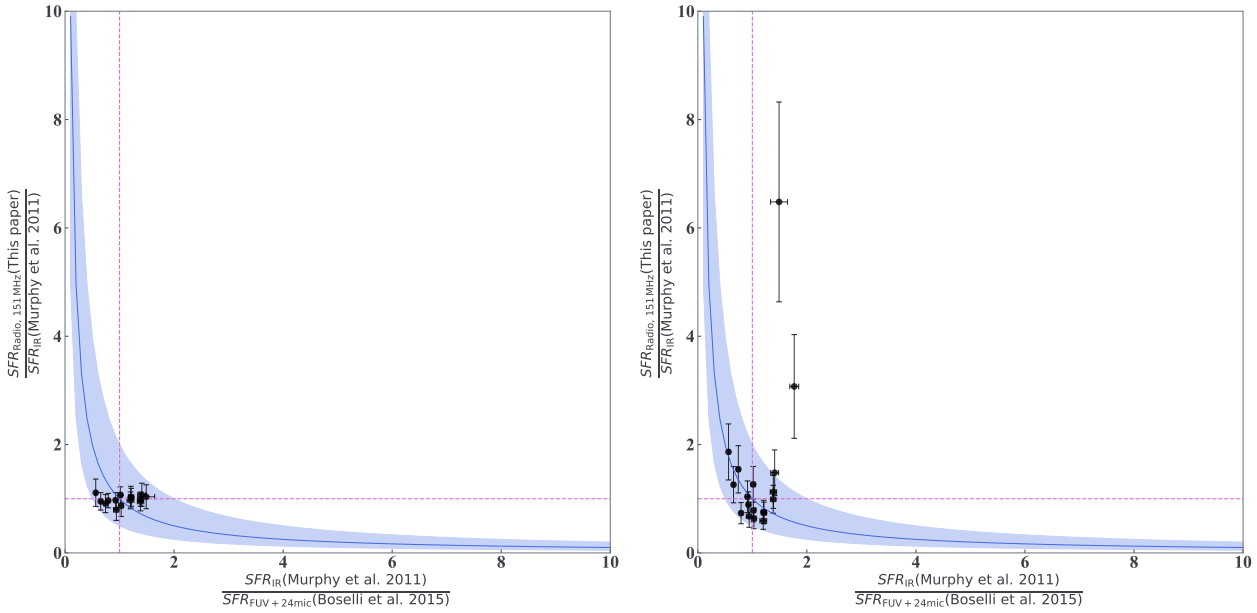


**Figure 5.4:** This figure shows SFR ratios from different indicators. The vertical and horizontal axes are  $SFR_{\text{Radio}, 151 \text{MHz}} / SFR_{\text{IR}}$  and  $SFR_{\text{IR}} / SFR_{\text{FUV} + 24\text{mic}}$  in both plots. Magenta dashed lines indicate the unity for each SFR ratio, and the solid blue lines do for the SFR ratio between  $SFR_{\text{Radio}, 151 \text{MHz}} / SFR_{\text{FUV} + 24\text{mic}}$ . The blue shaded region shows the ratio between  $SFR_{\text{Radio}, 151 \text{MHz}}$  and  $SFR_{\text{FUV} + 24\text{mic}}$  within factor two ( $0.5 \leq SFR_{\text{Radio}, 151 \text{MHz}} / SFR_{\text{FUV} + 24\text{mic}} \leq 2$ ). The difference between the upper and middle plots is the calibration parameters to calculate  $SFR_{\text{Radio}, 151 \text{MHz}}$ .

Figure 5.3 shows the SFR ratio between  $SFR_{\text{Radio}, \nu}$  and  $SFR_{\text{IR}}$ . For drawing the upper figure, we substitute the individual  $q_{1500 \text{ MHz}}$  and  $\gamma$  into Equation 4.6. We calculate  $SFR_{\text{Radio}, \nu}$  at each MWA frequency and plot the mean value. Note that the number of galaxies taken for the mean at each frequency is different because we use only high-quality fluxes. In this case, we can see it is consistent with  $SFR_{\text{IR}}$  within a 10% error. For the middle figure, we substitute the averaged  $q_{1500 \text{ MHz}}$  and  $\gamma$  instead of individual values. This calibration method yields larger scatters compared to the previous one. However,  $SFR_{\text{Radio}, \nu}$  is still consistent with  $SFR_{\text{IR}}$ . The bottom figure shows the SFR ratio comparison from different calibrations. In this figure, it is clear that SFR calculated from the averaged value has more extensive scatters than from the individual values.

These figures give us the idea that calculating radio SFR needs the spectral energy distribution for less uncertainty. For the spectral, we find that the single power-law assumption yields the radio SFR with the consistency within 10%, even including galaxies that might have a flatter spectral at low frequencies.

Figure 5.4 shows the comparison of SFR ratios. For both plots in the figure, vertical and horizontal axes show the ratio between  $SFR_{\text{Radio}, 151 \text{MHz}}$  and  $SFR_{\text{IR}}$ , between  $SFR_{\text{IR}}$  and  $SFR_{\text{FUV} + 24\text{mic}}$ , respectively. We use radio emission at 151 MHz because this is the only flux band that all our samples have high-quality data. Here, we check the consistency of the radio SFR with other SFR indicators. While  $SFR_{\text{IR}}$  traces the only dust emission,  $SFR_{\text{FUV} + 24\text{mic}}$  does the direct young massive stellar emission dust-corrected with the radiation at 24  $\mu\text{m}$  [Kennicutt & Evans, 2012; Murphy et al., 2011]. This figure shows how consistent the radio SFR is with this direct emission tracer.

## **5.2. STAR FORMATION RATE (SFR) FROM THE LOW-FREQUENCY EMISSION**

The difference between these plots is the calibration parameter for calculating  $\text{SFR}_{\text{Radio}, 151 \text{ MHz}}$ . The individual  $q_{1500 \text{ MHz}}$  and  $\gamma$  are used for the left plot and the averaged ones for the right plot. The blue shaded region shows the ratio between  $\text{SFR}_{\text{Radio}, 151 \text{ MHz}}$  and  $\text{SFR}_{\text{FUV}+24\text{mic}}$  within factor two ( $0.5 \leq \text{SFR}_{\text{Radio}, 151 \text{ MHz}} / \text{SFR}_{\text{FUV}+24\text{mic}} \leq 2$ ). In the figure, we can see that the radio SFR using individual parameters is also consistent with  $\text{SFR}_{\text{FUV}+24\text{mic}}$ . However, in the other case, there are two galaxies (HRS 306 and 144) whose radio SFR overestimates. This is because these galaxies have stronger radio emission (lower  $q_\nu$ ) than the extrapolated average value at 151 MHz.

# Chapter 6

## Discussions

### ABSTRACT

Intro intro intro intro.

### 6.1 Comparing the calibration with previous results

Here, we compare our results in Section ?? with previous research. From our samples, we obtain the mean  $\gamma = -0.63 \pm 0.07$  with MWA frequencies and 1500 MHz. Calistro Rivera et al. [2017] and Chyžý et al. [2018] obtained  $-0.78 \pm 0.24$  and  $-0.56 \pm 0.11$ , respectively. The difference of these might result from the selection of galaxy samples. While we use nearby galaxies within 25 Mpc, Calistro Rivera et al. [2017] do 758 galaxies up to  $z \sim 2$ , and Chyžý et al. [2018] do 118 galaxies up to  $z = 0.04$ .

Chyžý et al. [2018] indicate that the slope is steeper at higher frequencies ( $1.3 \sim 5$  GHz), and this might steepen the slope of galaxy samples in Calistro Rivera et al. [2017] which adopt galaxies up to  $z \sim 2$ . Considering the value and scatter, our result using the Herschel reference sample would be consistent with previous findings. Indeed, the frequency dependence of the low-frequency emission and its relation with IR emission is still uncertain.

### 6.2 Radio SFR uncertainty

In Section 5.2, we show the consistency of our SFR calibrations using the low-frequency emission. For calculating the more accurate radio SFR, we need its spectral energy distribution for each galaxy, as we have already shown in Section 5.2. Since star-forming galaxies have a wide variety of  $q_\nu$  at low frequencies ( $\sim 0.53$  dex in Figure 14, 15; Calistro Rivera et al. 2017), and still we do not know the physical details, the radio SFR calibration has considerable uncertainty. Substituting averaged  $\gamma$  and  $q_{1500\text{MHz}}$  obtained from our sample galaxies into Equation 4.6 yields the following equation:

$$\text{SFR}_{\text{Radio}, 150\text{MHz}} = (1.03 \pm 0.27) \times 10^{-29} \times \left( \frac{L_{\text{Radio}, 150\text{MHz}}}{\text{erg s}^{-1}} \right) \quad (6.1)$$

where we substitute the median values of  $\gamma = -0.63$ ,  $q_{1500\text{MHz}} = 2.48$  and  $\nu = 150$  MHz into Equation 4.6.

Calistro Rivera et al. [2017] have obtained the coefficient of  $0.76 \pm 0.08$  at  $z = 0$  (Equation 11) from their calibration.

We should keep our mind that the SFR calibration has non-negligible uncertainty, possibly caused by the galaxy selection and the variety of  $q_\nu$  at low frequencies. We need the radio spectral with multi-band observation for estimating SFR accurately.

# Chapter 7

## Summary

In this study, we investigate 18 star-forming galaxies in the HRS catalog for their global relation of the low-frequency radio with IR luminosities. We find a single power-law assumption for the frequency dependence of  $q_\nu$  is valid across MWA frequencies and 1.5 GHz, and their slope  $\gamma$  is consistent with previous studies. We also investigate the consistency of the radio SFR expected to be an extinction-free indicator. Our sample shows that the spectral information for each galaxy is needed to estimate its SFR accurately because of a wide variety of  $q_\nu$ . These results suggest that future observation with several radio bands is required at low frequencies for measuring accurate SFRs.

For further understanding of the low-frequency properties in star-forming galaxies, we need more samples from multi-band observation. The updated GLEAM survey will reveal physical details with an order of magnitude better angular-resolution and sensitivity than the latest survey.

# Bibliography

- Abazajian K. N., et al., 2009, *The Astrophysical Journal Supplement Series*, 182, 543
- Abolfathi B., et al., 2018, *The Astrophysical Journal Supplement Series*, 235, 42
- Baldwin A., Phillips M. M., Terlevich R., 1981, *Publications of the Astronomical Society of the Pacific*, 93, 817
- Bell E. F., 2003, *The Astrophysical Journal*, 586, 794
- Bendo G. J., Galliano F., Madden S. C., 2012, *Monthly Notices of the Royal Astronomical Society*, 423, 197
- Blumenthal G. R., Faber S. M., Primack J. R., Rees M. J., 1984, *Nature*, 311, 517
- Boselli A., et al., 2010, *Publications of the Astronomical Society of the Pacific*, 122, 261
- Boselli A., Cortese L., Boquien M., Boissier S., Catinella B., Lagos C., Saintonge A., 2014, *Astronomy and Astrophysics*, 564, 1
- Boselli A., Fossati M., Gavazzi G., Ciesla L., Buat V., Boissier S., Hughes T. M., 2015, *Astronomy & Astrophysics*, 579, A102
- Buat V., 1991, *Astrophysical Journal*, 376, 95
- Calistro Rivera G., et al., 2017, *Monthly Notices of the Royal Astronomical Society*, 469, 3468
- Carilli C. L., Holdaway M. A., Ho P. T. P., de Pree C. G., 1992, *The Astrophysical Journal*, 399, L59
- Chabrier G., 2003, *Publications of the Astronomical Society of the Pacific*, 115, 763
- Chyžý K. T., et al., 2018, *Astronomy & Astrophysics*, 619, A36
- Ciesla L., et al., 2012, *Astronomy & Astrophysics*, 543, A161
- Ciesla L., et al., 2014, *Astronomy & Astrophysics*, 565, A128
- Condon J. J., 1992, *Annual Review of Astronomy and Astrophysics*, 30, 575
- Condon J. J., Anderson M. L., Helou G., 1991, *The Astrophysical Journal*, 376, 95
- Cortese L., et al., 2012, *Astronomy & Astrophysics*, 544, A101

- Cortese L., et al., 2014, *Monthly Notices of the Royal Astronomical Society*, 440, 942
- For B.-Q., et al., 2018, *Monthly Notices of the Royal Astronomical Society*, 480, 2743
- Galametz M., et al., 2013, *Monthly Notices of the Royal Astronomical Society*, 431, 1956
- Giovanelli R., et al., 2005, *The Astronomical Journal*, 130, 2598
- Hao C.-N., Kennicutt R. C., Johnson B. D., Calzetti D., Dale D. A., Moustakas J., 2011, *The Astrophysical Journal*, 741, 124
- Haynes M. P., et al., 2011, *The Astronomical Journal*, 142, 170
- Heesen V., et al., 2019, *Astronomy & Astrophysics*, 622, A8
- Helou G., Soifer B. T., Rowan-Robinson M., 1985, *The Astrophysical Journal*, 298, L7
- Hopkins A. M., Beacom J. F., 2006, *The Astrophysical Journal*, 651, 142
- Hughes A., Staveley-Smith L., Kim S., Wolleben M., Filipovic M., 2007, *Monthly Notices of the Royal Astronomical Society*, 382, 543
- Hurley-Walker N., et al., 2017, *Monthly Notices of the Royal Astronomical Society*, 464, 1146
- Kapińska A. D., et al., 2017, *The Astrophysical Journal*, 838, 68
- Kauffmann G., et al., 2003, *Monthly Notices of the Royal Astronomical Society*, 346, 1055
- Kennicutt R. C., 1998, *Annual Review of Astronomy and Astrophysics*, 36, 189
- Kennicutt R. C., Evans N. J., 2012, *Annual Review of Astronomy and Astrophysics*, 50, 531
- Kennicutt R. C., et al., 2009, *Astrophysical Journal*, 703, 1672
- Kewley L. J., Dopita M. A., Sutherland R. S., Heisler C. A., Trevena J., 2001, *The Astrophysical Journal*, 556, 121
- Kroupa P., 2001, *Monthly Notices of the Royal Astronomical Society*, 322, 231
- Lequeux J., Maucherat-Joubert M., Deharveng J. M., Kunth D., 1981, *Astronomy and Astrophysics*, 103, 305L
- Madau P., Dickinson M., 2014, *Annual Review of Astronomy and Astrophysics*, 52, 415
- Martin D. C., et al., 2005, *The Astrophysical Journal*, 619, L1
- Murphy E. J., et al., 2011, *The Astrophysical Journal*, 737, 67
- Navarro J. F., Steinmetz M., 2000, *The Astrophysical Journal*, 528, 607
- Noll S., Burgarella D., Giovannoli E., Buat V., Marcillac D., Muñoz-Mateos J. C., 2009, *Astronomy & Astrophysics*, 507, 1793

- Padovani P., et al., 2017, *The Astronomy and Astrophysics Review*, 25, 2
- Peebles P. J. E., 1982, *The Astrophysical Journal*, 263, L1
- Read S. C., et al., 2018, *Monthly Notices of the Royal Astronomical Society*, 480, 5625
- Rieke G. H., et al., 2004, *The Astrophysical Journal Supplement Series*, 154, 25
- Salpeter E. E., 1955, *The Astrophysical Journal*, 121, 161
- Schawinski K., Thomas D., Sarzi M., Maraston C., Kaviraj S., Joo S.-J., Yi S. K., Silk J., 2007, *Monthly Notices of the Royal Astronomical Society*, 382, 1415
- Schlegel D. J., Finkbeiner D. P., Davis M., 1998, *The Astrophysical Journal*, 500, 525
- Schober J., Schleicher D. R. G., Klessen R. S., 2017, *Monthly Notices of the Royal Astronomical Society*, 468, 946
- Takeuchi T. T., Buat V., Iglesias-Páramo J., Boselli A., Burgarella D., 2005, *Astronomy & Astrophysics*, 432, 423
- Taylor A. R., Stil J. M., Sunstrum C., 2009, *The Astrophysical Journal*, 702, 1230
- Tingay S. J., et al., 2013, *Journal of Physics: Conference Series*, 440, 012033
- Tinsley B. M., Danly L., 1980, *The Astrophysical Journal*, 242, 435
- Urry C. M., Padovani P., 1995, *Publications of the Astronomical Society of the Pacific*, 107, 803
- Vale A., Ostriker J. P., 2004, *Monthly Notices of the Royal Astronomical Society*, 353, 189
- Völk H., 1989, *Astronomy and Astrophysics*, 218, 67
- Wang L., Gao F., Duncan K. J., Williams W., Rowan-Robinson M., Sabater J., Shimwell T. W., 2019, *Astronomy & Astrophysics*, 109, 1
- Yun M. S., Reddy N. A., Condon J. J., 2001, *The Astrophysical Journal*, 554, 803
- van Haarlem M. P., et al., 2013, *Astronomy & Astrophysics*, 556, A2

# Appendix A

## Galaxy images

### A.1 Matched samples (18 samples used for the analysis)

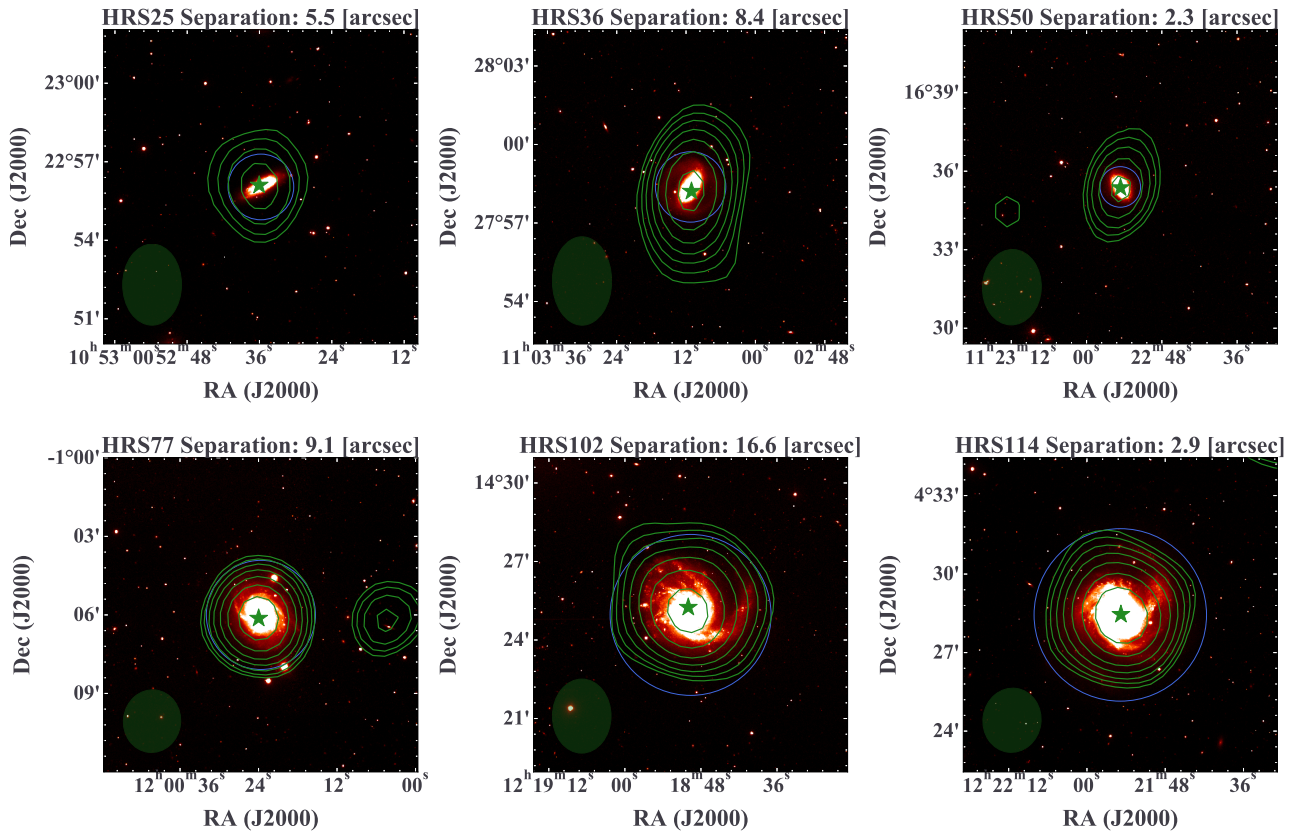


**Figure A.1:** These are the SDSS [Abolfathi et al., 2018] i-band images with radio contours from the GLEAM survey at 170 – 231 MHz (solid green lines). These galaxies are selected in Section 4.1 and 4.2. I draw the green contours started from the  $3\sigma$  local noise and increase by a factor of the square root of  $2^n$  (“n” is an integer). The green star marker shows the location of a radio source referred to as the GLEAM catalog. The size of this marker does not mean any feature of observations. The blue circle shows the isophotal optical size at 25 mag arcsec $^{-2}$  from Boselli et al. [2010]. On the bottom left in each plot, we show the beam size of the GLEAM survey.

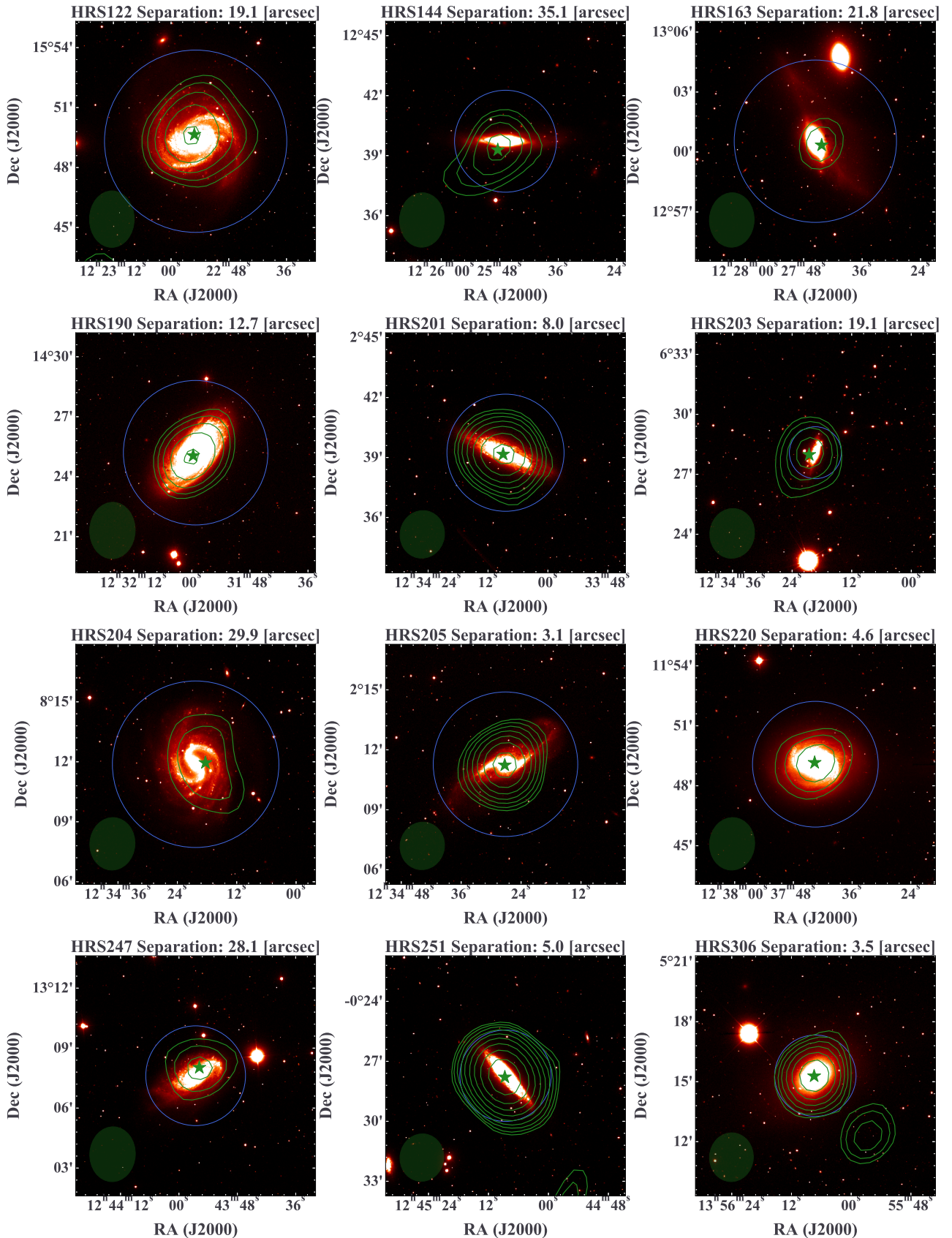


**Figure A.2:** Continuous.

## A.2 Matched samples (not used for the analysis)

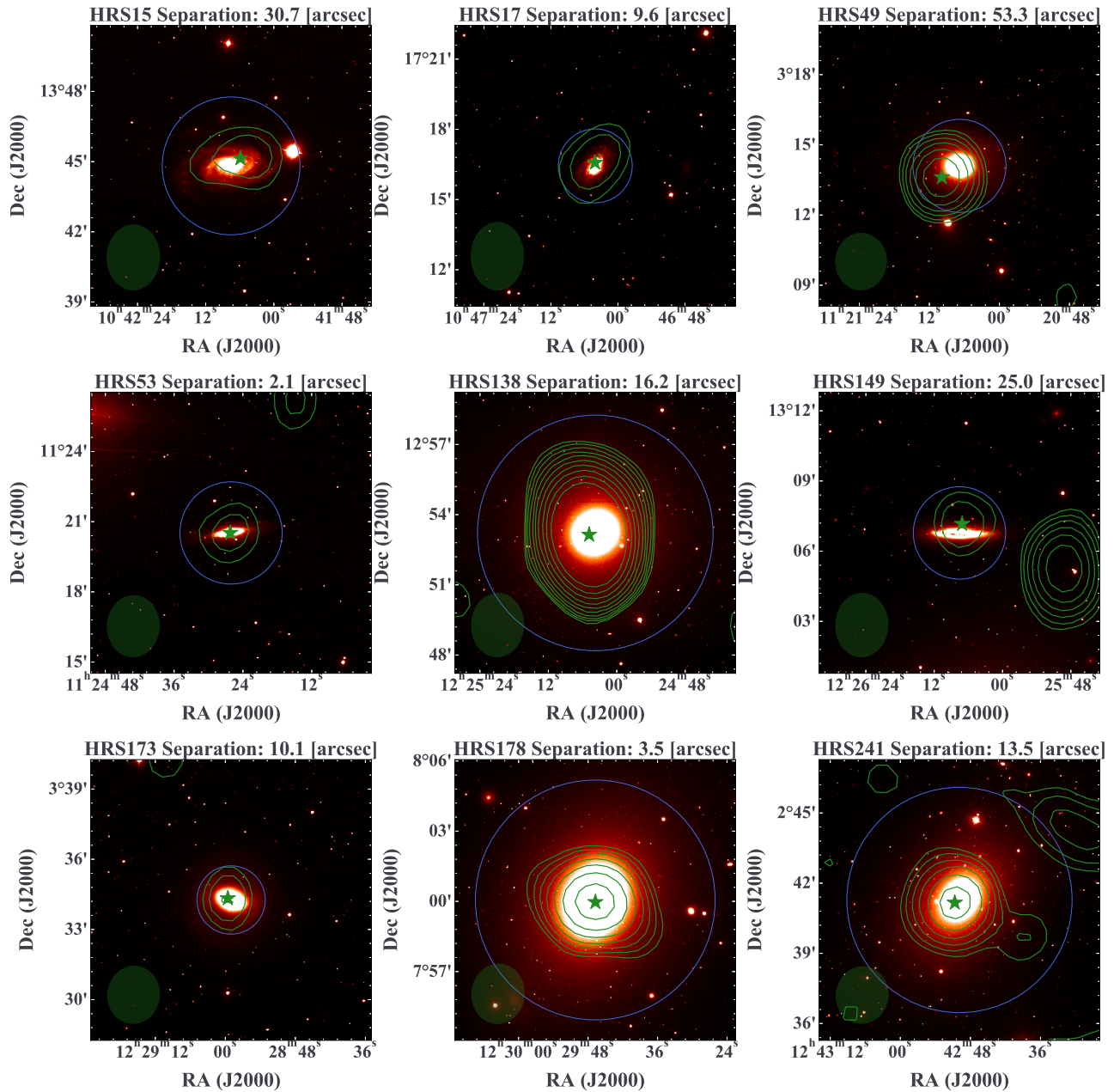


**Figure A.3:** These galaxies are not used for the analysis labeled in Section 4.2 although they have a radio counterpart in the GLEAM catalog by the cross-matching.

## A.3 Suspicious matching samples

## A.4 Not matching samples

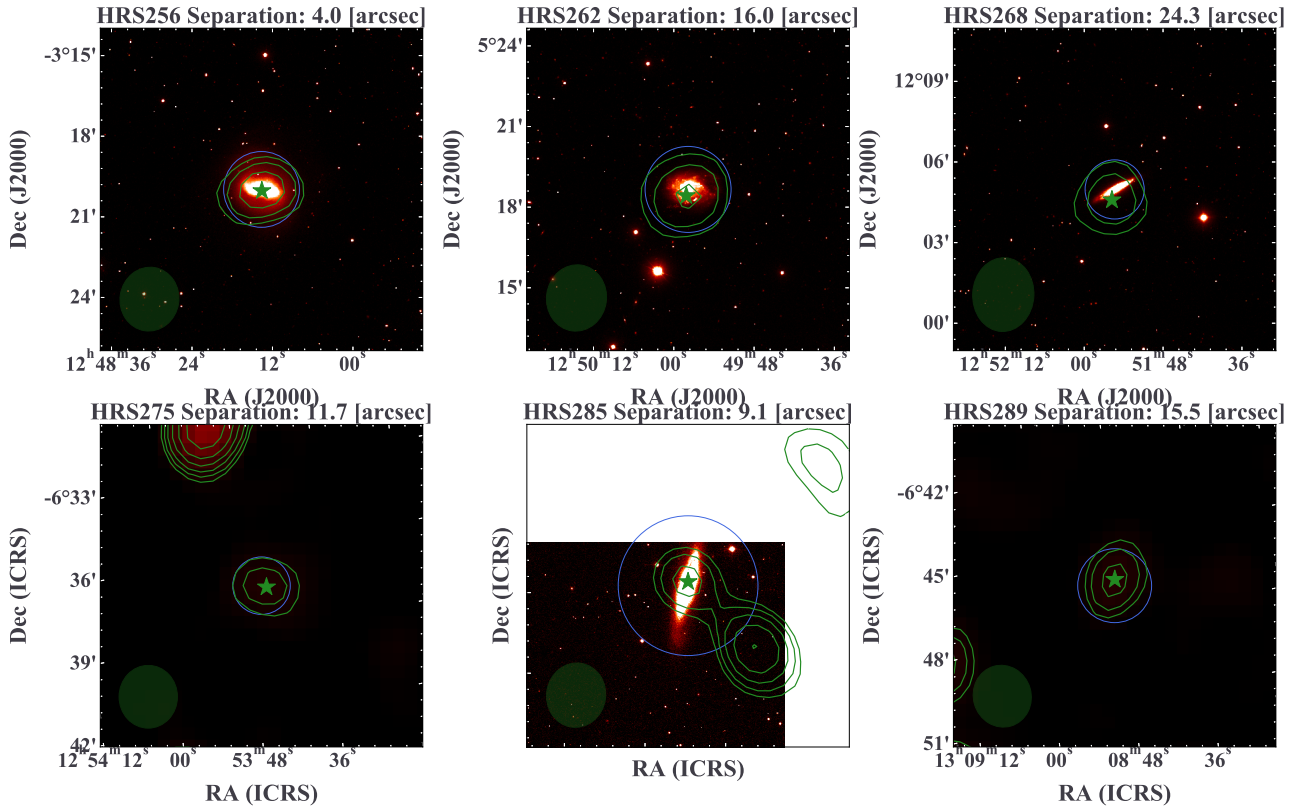


Figure A.4: Continuous.

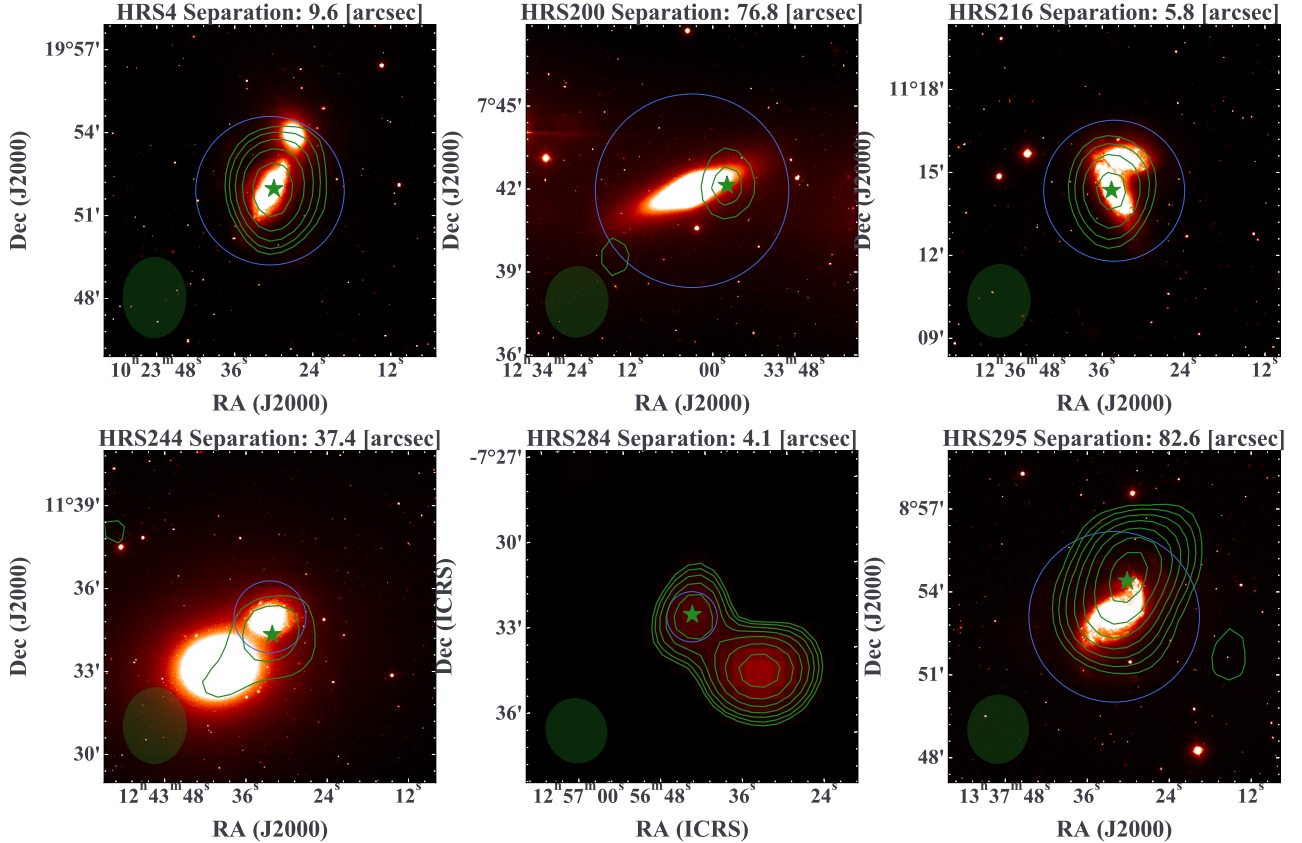
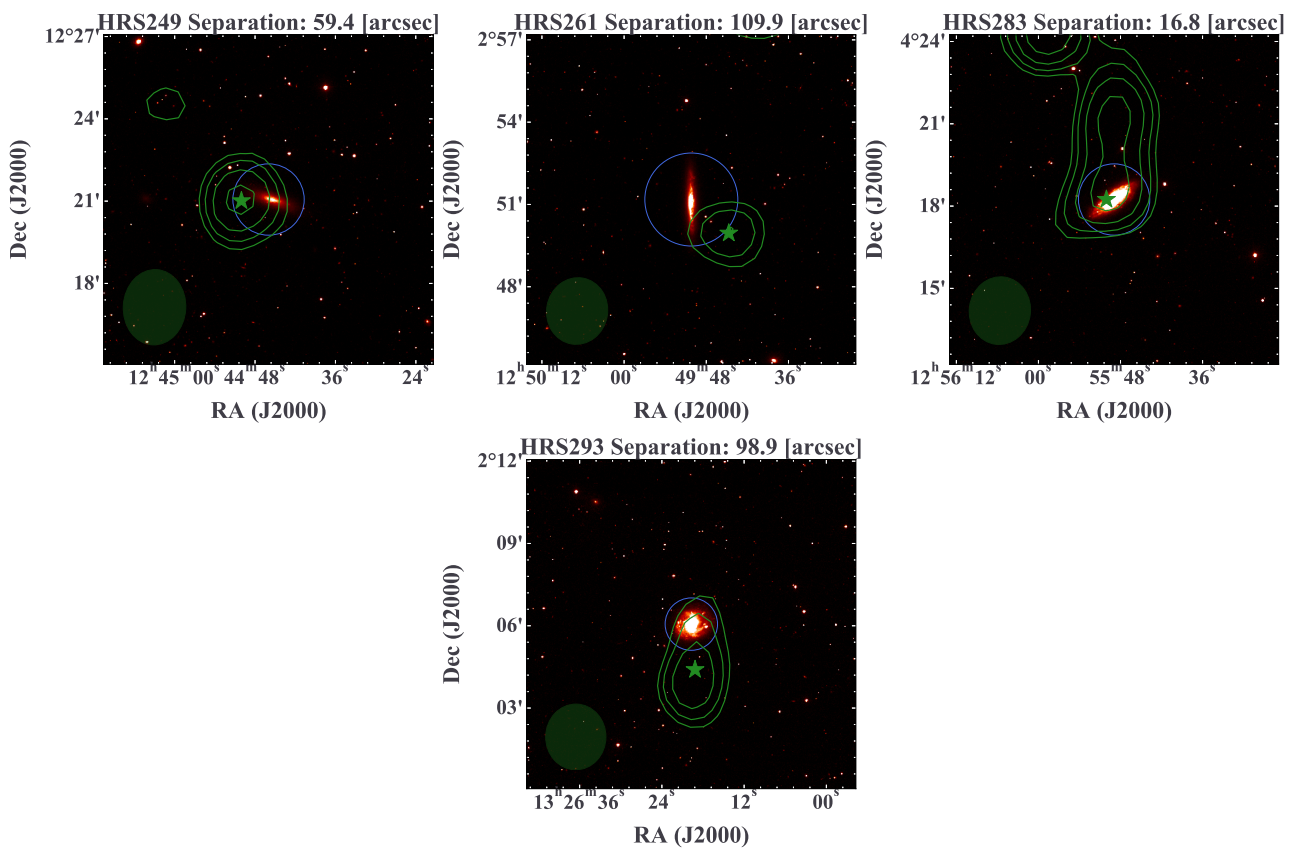


Figure A.5: These galaxies are flagged as a suspicious matching in Section 4.1



**Figure A.6:** These galaxies do not have a radio counterpart from the GLEAM catalog in Section 4.1

## Appendix B

### Galaxy samples for the analysis

**Table B.1:** This table shows 18 HRS galaxies selected in Section ???. Column (1) NGC (2) R.A. (3) Dec. (5) D25 (6) Dist. are from Cortese et al. [2012], column (4) Type is from Ciesla et al. [2014] (Cortese et al. 2012 for only HRS 163) and column (7) GLEAM ID refers to GLEAM catalog.  $\alpha_{\text{MWA}}$ ,  $\alpha_{\text{MWA+1500MHz}}$  are the result in Section ???.  $\text{SFR}_{\text{IR}}$  is calculated with the equation from Murphy et al. [2011] and  $\text{SFR}_{\text{Radio, 151MHz}}$  is calculated in Section ?? with individual parameters. “AGN” is identified BPT diagram [e.g. Baldwin et al., 1981; Kauffmann et al., 2003; Kewley et al., 2001; Schawinski et al., 2007] with emission lines [Boselli et al., 2015]. HI deficient galaxy is identified when the value of HI-def [Boselli et al., 2014] is larger than 0.4.

NGC HRS	R.A.	Dec	Type	D25 [arcmin]	Dist. [Mpc]	GLEAM ID	$\alpha_{\text{MWA}}$	$\alpha_{\text{MWA+1500MHz}}$	$\text{SFR}_{\text{IR}}$ [ $M_{\odot} \text{ yr}^{-1}$ ]	$\text{SFR}_{\text{Radio, 151MHz}}$ [ $M_{\odot} \text{ yr}^{-1}$ ]	AGN	HI-def	
25	3437	10:52:35.75	+22:56:02.9	Sc	2.51	18.24	J105236+225606	0.33+/-0.47	-0.66+/-0.07	1.41+/-0.08	0.96+/-0.28	-	-
36	3504	11:03:11.21	+27:58:21.0	Sab	2.69	21.94	J110311+275812	-0.42+/-0.1	-0.53+/-0.05	4.09+/-0.16	5.15+/-1.35	-	True
50	3655	11:22:54.62	+16:35:24.5	Sc	1.55	21.43	J112254+163522	-0.38+/-0.2	-0.63+/-0.04	1.91+/-0.07	1.45+/-0.41	-	-
77	4030	12:00:23.64	-01:06:00.0	Sbc	4.17	20.83	J120023-010607	-0.57+/-0.07	-0.63+/-0.04	4.81+/-0.19	3.55+/-0.94	-	-
102	4254	12:18:49.63	+14:24:59.4	Sc	6.15	17.00	J121850+142515	-0.7+/-0.05	-0.7+/-0.03	6.47+/-0.25	8.19+/-2.12	-	-
114	4303	12:21:54.90	+04:28:25.1	Sbc	6.59	17.00	J122154+042827	-0.57+/-0.05	-0.58+/-0.04	6.15+/-0.23	5.49+/-1.43	-	-
122	4321	12:22:54.90	+15:49:20.6	Sbc	9.12	17.00	J122255+154939	-0.77+/-0.07	-	5.45+/-0.22	4.28+/-1.14	-	True
144	4388	12:25:46.82	+12:39:43.5	Sb	5.10	17.00	J122548+123917	0.22+/-0.22	-0.73+/-0.08	1.66+/-0.06	3.09+/-0.85	Seyfert	True
163	4438	12:27:45.59	+13:00:31.8	Sb	8.12	17.00	J122744+130020	-0.81+/-0.35	-	0.69+/-0.03	2.13+/-0.66	Seyfert	True
190	4501	12:31:59.22	+14:25:13.5	Sb	7.23	17.00	J123159+142503	-0.67+/-0.12	-0.72+/-0.05	4.37+/-0.18	4.92+/-1.31	-	True
201	4527	12:34:08.50	+02:39:13.7	Sbc	5.86	17.00	J123408+023909	-0.54+/-0.06	-0.56+/-0.04	4.55+/-0.24	2.71+/-0.71	-	-
203	4532	12:34:19.33	+06:28:03.7	Im(Im/S)	2.60	17.00	J123420+062758	-0.55+/-0.13	-0.6+/-0.04	0.99+/-0.04	1.52+/-0.43	-	-
204	4535	12:34:20.31	+08:11:51.9	Sc	8.33	17.00	J123418+081157	-0.71+/-0.1	-	2.6+/-0.11	2.69+/-0.75	-	-
205	4536	12:34:27.13	+02:11:16.4	Sbc	7.23	17.00	J123427+021114	-0.61+/-0.04	-0.57+/-0.02	3.58+/-0.14	2.63+/-0.69	-	-
220	4579	12:37:43.52	+11:49:05.5	Sb	6.29	17.00	J123743+114909	-0.42+/-0.18	-0.77+/-0.05	1.56+/-0.08	2.32+/-0.65	LINER	True
247	4654	12:43:56.58	+13:07:36.0	Scd	4.99	17.00	J124355+130801	-0.27+/-0.29	-0.66+/-0.06	2.59+/-0.11	1.65+/-0.49	-	-
251	4666	12:45:08.59	-00:27:42.8	Sc	4.57	21.61	J124508-002747	-0.58+/-0.03	-0.58+/-0.02	9.2+/-0.33	9.11+/-2.35	-	-
306	5363	13:56:07.21	+05:15:17.2	pec	4.07	16.23	J135607+051516	-0.61+/-0.08	-0.51+/-0.04	0.27+/-0.03	1.75+/-0.46	-	True